

Search for binary black hole mergers in the third observing run of Advanced LIGO-Virgo using coherent WaveBurst enhanced with machine learning

T. Mishra¹, B. O'Brien¹, M. Szczepańczyk¹, G. Vedovato², S. Bhaumik¹, V. Gayathri¹, G. Prodi^{3,4},
F. Salemi^{5,4}, E. Milotti^{6,7}, I. Bartos¹, and S. Klimenko¹

¹*Department of Physics, University of Florida, PO Box 118440, Gainesville, Florida 32611-8440, USA*

²*INFN, Sezione di Padova, I-35131 Padova, Italy*

³*Università di Trento, Dipartimento di Matematica, I-38123 Povo, Trento, Italy*

⁴*INFN, Trento Institute for Fundamental Physics and Applications, I-38123 Povo, Trento, Italy*

⁵*Università di Trento, Dipartimento di Fisica, I-38123 Povo, Trento, Italy*

⁶*Università di Trieste, Dipartimento di Fisica, I-34127 Trieste, Italy*

⁷*INFN, Sezione di Trieste, I-34127 Trieste, Italy*



(Received 28 January 2022; accepted 28 March 2022; published 26 April 2022)

In this work, we use the coherent WaveBurst (cWB) pipeline enhanced with machine learning (ML) to search for binary black hole (BBH) mergers in the Advanced LIGO-Virgo strain data from the third observing run. We detect, with equivalent or higher significance, all gravitational-wave (GW) events previously reported by the standard cWB search for BBH mergers in the third GW Transient Catalog. The ML-enhanced cWB search identifies five additional GW candidate events from the catalog that were previously missed by the standard cWB search. Moreover, we identify three marginal candidate events not listed in third GW Transient Catalog. For simulated events distributed uniformly in a fiducial volume, we improve the sensitive hypervolume with respect to the standard cWB search by approximately 28% and 34% for the stellar-mass and intermediate mass black hole binary mergers respectively, detected with a false-alarm rate less than $1/100 \text{ yr}^{-1}$. We show the robustness of the ML-enhanced search for detection of generic BBH signals by reporting increased sensitivity to the spin-precessing and eccentric BBH events as compared to the standard cWB search. Furthermore, we compare the improvement of the ML-enhanced cWB search for different detector networks.

DOI: [10.1103/PhysRevD.105.083018](https://doi.org/10.1103/PhysRevD.105.083018)

I. INTRODUCTION

The Advanced LIGO [1] and Advanced Virgo [2] network of detectors detected 11 gravitational-wave (GW) candidates during the first two observing runs (O1 and O2) [3], 44 GW candidates in the first half of the third observing run (O3a) [4,5], and 35 GW candidates during the second half of the third observing run (O3b) [6]. These detections were identified by the different search pipelines employed by the LIGO-Virgo-KAGRA (LVK) collaboration, including GstLAL [7–9], PyCBC [10–12], MBTA [13], and coherent WaveBurst (cWB) [14,15].

cWB is a search algorithm that looks for excess power in the time-frequency domain to identify GW signals in the LIGO-Virgo strain data [14–18]. Unlike matched-filter based pipelines, cWB does not explicitly use signal waveform models, making it a minimally modeled search. Thus, the cWB pipeline is expected to play an integral role in the detection of poorly modeled or unexpected GW sources. Historically, cWB was crucial for the discovery of the first binary black hole (BBH) merger GW150914 [19], which initiated the era of GW astronomy. More recently, cWB contributed in the identification of higher multipoles for

GW190814 [20,21], an event associated with the coalescence of a binary system with the most unequal mass ratio yet measured with gravitational waves. cWB was also instrumental to the first direct detection of an intermediate mass black hole (IMBH) GW190521 [22,23], which is the most massive and distant black hole merger observed via GWs. Overall, the cWB pipeline has contributed to the detection of 32 BBH events in the O1, O2, and O3 observing runs [3,4,6].

The cWB algorithm has been recently used in combination with machine learning (ML) algorithms for various studies [24–27]. In this paper, the standard cWB pipeline sensitivity to BBH mergers is enhanced by using the ML method as described in Ref. [28]. We reanalyze the publicly available strain data from O3 [29] using the ML-enhanced cWB pipeline for the two-fold detector network consisting of LIGO Hanford and LIGO Livingston (HL). We optimize the ML-enhanced cWB search for the three-fold detector network consisting of LIGO Hanford, LIGO Livingston, and Virgo (HLV), where we analyze limited data from O3 to compare the performance with the two-fold detector network and discuss possible causes for suboptimality of the three-fold detector network.

The paper is organized as follows. In Sec. II, we introduce the ML-enhanced cWB search pipeline and discuss the updates to the method. Section II B describes the data used to train and test our ML algorithm. We present the results of the O3 data reanalysis with the ML-enhanced cWB in Sec. III. Section III A reports the updated significance of BBH events detected during the O3 run. Section III B discusses the marginal events found in this reanalysis, followed by the comparison of search sensitivity of the ML-enhanced cWB search against the sensitivity of the standard cWB search in Sec. III C. The tests of robustness of the ML method are given in Sec. III D and Sec. III E compares the performance of the ML method on different network configurations. Finally, in Sec. IV, we state the conclusions of the ML-enhanced cWB search for binary mergers on O3.

II. METHOD

A. Coherent WaveBurst

The cWB pipeline searches for transient GW signals by identifying events with excess power in the time-frequency domain. cWB reconstructs coherent events in multiple detectors with minimal assumptions on the signal model [14,15]. The time-frequency domain data is built from the detector strain data by using the Wilson Daubechies Meyer (WDM) wavelet transform [30]. The algorithm identifies events by clustering the nearby WDM wavelets with excess power above the average fluctuations of the detector noise. The pipeline generates an event for each selected cluster and reconstructs the signal waveform using the constrained maximum likelihood method [15]. The cWB pipeline estimates various summary statistics for each event, describing the time-frequency structure, signal strength, and coherence across the detector network. The standard cWB detection statistic used to identify the GW events has been updated with respect to previous searches as given below:

$$\eta_0 = \sqrt{\frac{E_c}{1 + \chi^2(\max(1, \chi^2) - 1)}}, \quad (1)$$

Here, χ^2 is given by $\chi^2 = E_n/N_{\text{df}}$ where E_n is the estimated residual noise energy, and N_{df} is the number of independent wavelet amplitudes describing the event. The χ^2 factor is close to unity for genuine GW events and penalizes the non-Gaussian noise contribution. The coherent energy E_c , is estimated by cross-correlating the reconstructed signal waveforms across different detectors. In the standard cWB analysis, the significance of GW events is increased by removing the excess background with *a priori* defined veto conditions on a set of summary statistics generated for each event [4,23,31]. Although this method works well, it may entirely remove the borderline GW events which do not pass the veto thresholds. The veto conditions need to be

manually tuned for each observing run and detector network. Moreover, designing these veto conditions in the multidimensional space of the summary statistics is challenging. Using the ML method, allows us to automate and enhance the separation of signal and noise events while simultaneously increasing the sensitivity of the search [28]. In the ML-enhanced cWB pipeline, we define the reduced detection statistic given by:

$$\eta_r = \eta_0 \cdot W_{\text{XGB}}, \quad (2)$$

where W_{XGB} is the penalty factor provided by the ML algorithm [28].

In the standard cWB search, we employ two different search configurations to improve the search sensitivity: the BBH configuration targeting stellar-mass BBH mergers ($M_{\text{tot}} \lesssim 100 M_{\odot}$) and the IMBH configuration targeting intermediate mass black hole (IMBH) binary mergers ($M_{\text{tot}} \gtrsim 100 M_{\odot}$). The corresponding GW signals observed in the LIGO frequency band are quite different for the two systems. A GW signal originating from the stellar-mass BBH merger and observable in the LIGO bandwidth usually exhibits the entire inspiral-merger-ringdown waveform. In contrast, GW signals from IMBH binary mergers are short in duration and contain mostly the merger-ringdown waveform, with the inspiral signal buried inside the low-frequency seismic noise. A specialized search for IMBH mergers helps to constrain the PISN mass gap [32] and possible formation channels [33] for massive binaries.

The estimated central frequency f_0 of a GW signal is inversely proportional to the redshifted total mass of the binary system. As a result, IMBH binaries are expected to merge at lower frequencies than the stellar-mass BBH mergers. So, we select events with $60 \text{ Hz} < f_0 < 300 \text{ Hz}$ for the BBH search configuration and events with $f_0 < 200 \text{ Hz}$ for the IMBH search configuration. Since the two search configurations overlap in the frequency bands, we combine them in accordance with the rules explained in Table 1 of Ref. [23].

B. Data

We analyze publicly available strain data from Advanced LIGO and Advanced Virgo's third observational run [29]. In order to train and test a supervised ML algorithm, we generate two types of data: noise events (background) and signal events (simulations). We accumulate the background data by time-shifting the data from one detector with respect to other detectors in the network. For data segments corresponding to live times of approximately 10 days, as many as $\mathcal{O}(100,000)$ time shifts are performed where each time shift is selected to be a multiple of one second. The time-shifted data is analyzed with the cWB pipeline to estimate the characteristics of the background events. To generate the simulation data, we inject simulated GW

signals into the detector data and recover these signals using the cWB pipeline. In this study, we use four sets of simulations: (i) a spin-aligned stellar-mass BBH set with quasicircular orbit approximation, (ii) a numerical relativity (NR) IMBH binary set, (iii) an eccentric BBH set, and (iv) a precessing BBH set with quasicircular orbit approximation. The binary orientation parameters (sky location, inclination angle) for every simulated waveform are randomly drawn from uniform distributions in all four cases. The redshift z is drawn from a uniform distribution in comoving volume, assuming Planck 2015 cosmology [34]. Simulation sets (i) and (ii) are used to train and test the ML algorithm, whereas the remaining two sets are only used to test the robustness of the ML implementation.

In the simulation set (i), the component black hole masses are drawn from models representing the stellar-mass BBH population [35,36]. The source frame total mass for these simulations ranges from approximately $5 M_{\odot}$ to $100 M_{\odot}$, and the mass ratios range from 1 to $1/4$. We use the SEOBNRv4 [37] waveform approximant to generate the simulations. The spins of the component black holes are drawn from a uniform, aligned spin distribution in the range -0.99 to 0.99 . The binary source distance is randomly drawn, assuming the uniform density in comoving volume.

For simulation set (ii), we use NR waveforms, including higher-order harmonics, as the representative models for IMBH binary set. We consider 17 mass bins, as described in Ref. [38], ranging in the source frame total mass from $120 M_{\odot}$ to $800 M_{\odot}$, and with mass ratios ranging from 1 to $1/10$.

In simulation set (iii), we also use NR waveforms for the high mass, eccentric BBH set [39,40]. We consider 28 mass bins ranging in total mass from $100 M_{\odot}$ to $250 M_{\odot}$, with mass ratio equal to 1, and eccentricities ranging from 0.01 to 0.96.

For the simulation set (iv) involving precessing stellar-mass BBH, we use the SEOBNRv4PHM [41] waveform approximant, which includes precession and the higher-order harmonic modes. The source frame total mass ranges from $4 M_{\odot}$ to $200 M_{\odot}$, with mass ratios ranging from 1 to $1/20$. The spins of the component black holes are isotropically distributed.

The amount of simulation and accumulated background data used for training and testing the ML algorithm is described in Table I.

C. XGBoost

We describe the procedure followed to train the ML algorithm and discuss updates on the method described in Ref. [28]. Here, we use an ensemble learning, boosted decision-tree based ML algorithm called XGBoost [42]. We start by selecting the subset of the cWB summary statistics used as the list of input features for training and testing the XGBoost algorithm. The data is split into training and testing as defined in Table I, and we train

TABLE I. Amount of accumulated background data (given in years) and the number of simulated events used for training and testing. We consider the third observing run (O3) for the two detector network (HL), search configurations (BBH, IMBH), and additional simulation cases from O3a to test the model robustness (Eccentric BBH, Precessing BBH). For the network study, we also consider limited BBH data (corresponding to 7 days of live time in the O3 run) for the three detector network (HLV).

O3 Dataset	Background (yr)		Simulation (events)	
	Training	Testing	Training	Testing
BBH	2000	28527	20077	110861
IMBH	2000	28535	19801	192626
Eccentric BBH	...	19101	...	974576
Precessing BBH	...	19093	...	17483
Network Study	550	639	1998	1992

two different models over the entire O3 run for the HL network: BBH search configuration and IMBH search configuration. For the detector network comparison discussed in Sec. III E, we train a BBH search configuration model for the HLV network with half of the limited data (GPS: 1241011102.0 to GPS: 1242485126) which corresponds to approximately 7 days of live time, given in Table III. We test the trained models on the remaining background and simulation data for each search type, apply these models to the GW candidate events in O3, and present the results in Sec. III.

The ML training and testing method utilized in this paper is consistent with the one presented in Ref. [28] except for the following changes: change in the subset of summary statistics used as the input features for XGBoost, the values of the XGBoost hyperparameters used for training the models, the introduction of the standardized sample weight. These updates to the existing method are discussed in Appendix.

III. RESULTS

In this section, we discuss the results of the ML-enhanced cWB search on O3 data. We first report the detections in Sec. III A, followed by the discussion of marginal events in Sec. III B. In Sec. III C, the improvement in the search sensitivity is discussed. We include tests of robustness to check the ML implementation in Sec. III D. Lastly, we compare the performance of searches with different detector networks in Sec. III E.

A. Search results

We train two separate models over the entire O3 run, one for the BBH search configuration and the other for the IMBH search configuration. The trained models are used to calculate the W_{XGB} , which is required for the estimation of the reduced detection statistic η_r [defined in Eq. (2)] for all candidate events. The detection statistic provides the

TABLE II. O3 ML-enhanced cWB search results compared with the standard cWB results. We report all detections with $\text{FAR} \leq 1 \text{ yr}^{-1}$ and present in the catalog papers [4,6]. The estimated significance is limited by the accumulated background data and is indicated with a ‘<’ entry. For the ML-enhanced cWB search, the background data used for training the ML model has been removed from the total available accumulated background data. We estimate the P_{astro} and report it along with the SNR reconstructed by the cWB pipeline for the GW events.

Event	Standard cWB	ML-enhanced cWB	SNR	P_{astro}
	FAR (yr^{-1})	FAR (yr^{-1})		
GW190408_181802	$<9.5 \times 10^{-4}$	$<1.0 \times 10^{-3}$	14.8	0.999
GW190412	$<9.5 \times 10^{-4}$	$<1.0 \times 10^{-3}$	19.7	0.999
GW190421_213856	3.0×10^{-1}	1.8×10^{-2}	9.3	0.997
GW190503_185404	1.8×10^{-3}	$<9.9 \times 10^{-4}$	11.5	0.999
GW190512_180714	3.0×10^{-1}	1.8×10^{-1}	10.7	0.941
GW190513_205428	...	$1.0 \times 10^{+0}$	11.5	0.703
GW190517_055101	6.5×10^{-3}	6.2×10^{-4}	10.7	0.999
GW190519_153544	3.1×10^{-4}	$<1.0 \times 10^{-4}$	14.0	1.000
GW190521	2.0×10^{-4}	$<1.0 \times 10^{-4}$	14.4	1.000
GW190521_074359	$<1.0 \times 10^{-4}$	$<1.0 \times 10^{-4}$	24.7	0.999
GW190602_175927	1.5×10^{-2}	$<8.8 \times 10^{-4}$	11.1	0.999
GW190701_203306	5.5×10^{-1}	1.1×10^{-2}	10.2	0.997
GW190706_222641	$<1.0 \times 10^{-3}$	$<1.1 \times 10^{-3}$	12.7	0.999
GW190707_093326	...	1.1×10^{-1}	11.2	0.976
GW190727_060333	8.8×10^{-2}	3.4×10^{-3}	11.4	0.998
GW190728_064510	...	2.6×10^{-2}	10.5	0.993
GW190828_063405	$<9.6 \times 10^{-4}$	$<1.1 \times 10^{-3}$	16.6	0.999
GW190915_235702	$<1.0 \times 10^{-3}$	$<1.1 \times 10^{-3}$	12.3	0.999
GW190929_012149	...	7.7×10^{-1}	9.2	0.542
GW191109_010717	$<1.1 \times 10^{-3}$	$<1.2 \times 10^{-3}$	15.6	0.999
GW191127_050227	...	2.1×10^{-1}	8.6	0.957
GW191204_171525	$<8.7 \times 10^{-4}$	$<9.6 \times 10^{-4}$	17.1	0.999
GW191215_223052	1.2×10^{-1}	$<9.6 \times 10^{-4}$	9.8	0.998
GW191222_033537	$<8.9 \times 10^{-4}$	$<9.8 \times 10^{-4}$	11.1	0.999
GW191230_180458	5.0×10^{-2}	2.0×10^{-3}	10.3	0.998
GW200128_022011	$1.3 \times 10^{+0}$	2.2×10^{-2}	8.8	0.985
GW200219_094415	7.7×10^{-1}	2.7×10^{-1}	10.4	0.887
GW200224_222234	$<8.8 \times 10^{-4}$	$<9.7 \times 10^{-4}$	18.8	0.999
GW200225_060421	$<8.8 \times 10^{-4}$	$<9.7 \times 10^{-4}$	13.1	0.999
GW200311_115853	$<8.2 \times 10^{-4}$	$<8.9 \times 10^{-4}$	16.2	0.999

ranking of detected events and allows the calculation of the false-alarm rate (FAR), which is used to assign the significance of a candidate event. The FAR value is estimated by counting the number of background events with an equal or higher value of the detection statistic than for the given candidate event, divided by the total available background time.

Table II reports the BBH candidates identified by the ML-enhanced cWB search in the O3 observing run. We identify with equivalent or higher significance all 15 + 10 (O3a + O3b) BBH candidates previously reported by the standard cWB search [4,6]. Moreover, the ML-enhanced cWB search detected GW190513, GW190707, GW190728, GW190929, and GW191127 with FAR of $<1 \text{ yr}^{-1}$, which were previously vetoed in the standard cWB search, but detected by the other search pipelines [4,6].

Three cWB-only marginal candidate events, not listed in the LVK catalogs, were also found by the ML-enhanced cWB search over O3 and are discussed in subsection III B. For all the GW and marginal candidate events in O3, we compute the corresponding probabilities of astrophysical origin (P_{astro}) assuming that the terrestrial and astrophysical events occur as independent Poisson processes [6,43].

B. Marginal candidate events

In GWTC-3, the cWB search had reported three marginal events, namely 190804_083543, 190930_234652, and 200214_224526 [6]. These events were identified by the standard cWB pipeline and are consistent with noise artifacts found around their GPS times. The ML-enhanced cWB search also identifies these events but assigns them a lower significance: 190804_083543 with a FAR of 28 yr^{-1} ,

TABLE III. Marginal cWB-only events were found in O3 with the ML-enhanced cWB search compared with the standard cWB analysis. We report all detections with FAR $< 1 \text{ yr}^{-1}$ not present in the catalog papers. We estimate the P_{astro} , cWB source frame total mass (M_{cWB}) and report it along with the SNR reconstructed by the cWB pipeline for the marginal events. We report the median and 90% symmetric credible intervals for the one-dimensional marginal posterior distributions of the source total mass M , and the source component masses: m_1 and m_2 . *190904_174910 is likely to be produced by the up-conversion of seismic noise and the 60 Hz power line.

Event	Standard cWB FAR (yr^{-1})	ML-enhanced cWB FAR (yr^{-1})	SNR	P_{astro}	$M_{\text{cWB}} (M_{\odot})$	$M (M_{\odot})$	$m_1 (M_{\odot})$	$m_2 (M_{\odot})$
190421_012633	$7.1 \times 10^{+0}$	4.4×10^{-1}	9.6	0.833	160	155^{+65}_{-32}	111^{+61}_{-38}	44^{+25}_{-20}
190904_174910*	...	8.5×10^{-1}	8.1	0.573
191223_151007	...	4.3×10^{-1}	7.5	0.742	141	206^{+55}_{-39}	153^{+43}_{-38}	54^{+27}_{-19}

190930_234652 with a FAR of 8 yr^{-1} , and 200214_224526 with a FAR of 17 yr^{-1} . The significance of these events is below the analysis threshold of FAR $< 1 \text{ yr}^{-1}$, and hence, they are not included in this paper. Instead, in Table III, we report the GW candidate events that are not present in the GW Transient Catalog papers but were detected by the ML-enhanced cWB search with FAR $< 1 \text{ yr}^{-1}$. The lowest-ranked event 190904_174910 is detected with a FAR of 0.85 yr^{-1} and reconstructed SNR of 8.5. The event 190904_174910 is not reconstructed by

the cWB pipeline when reanalysed with the sub60 Hz clean data (conditioned for the 60 Hz instrumental noise). Therefore, the event is likely to be associated with the instrumental noise produced around the 60 Hz line by the coupling of the low-frequency seismic noise [44–46].

The other two cWB-only events, 190421_012633 and 191223_151007 are marginal events detected with the FAR of $< 0.44 \text{ yr}^{-1}$ and $< 0.43 \text{ yr}^{-1}$ and reconstructed SNR of 9.6 and 7.5, respectively. The time-frequency wavescan spectrograms [47] of these events are shown in Fig. 1.

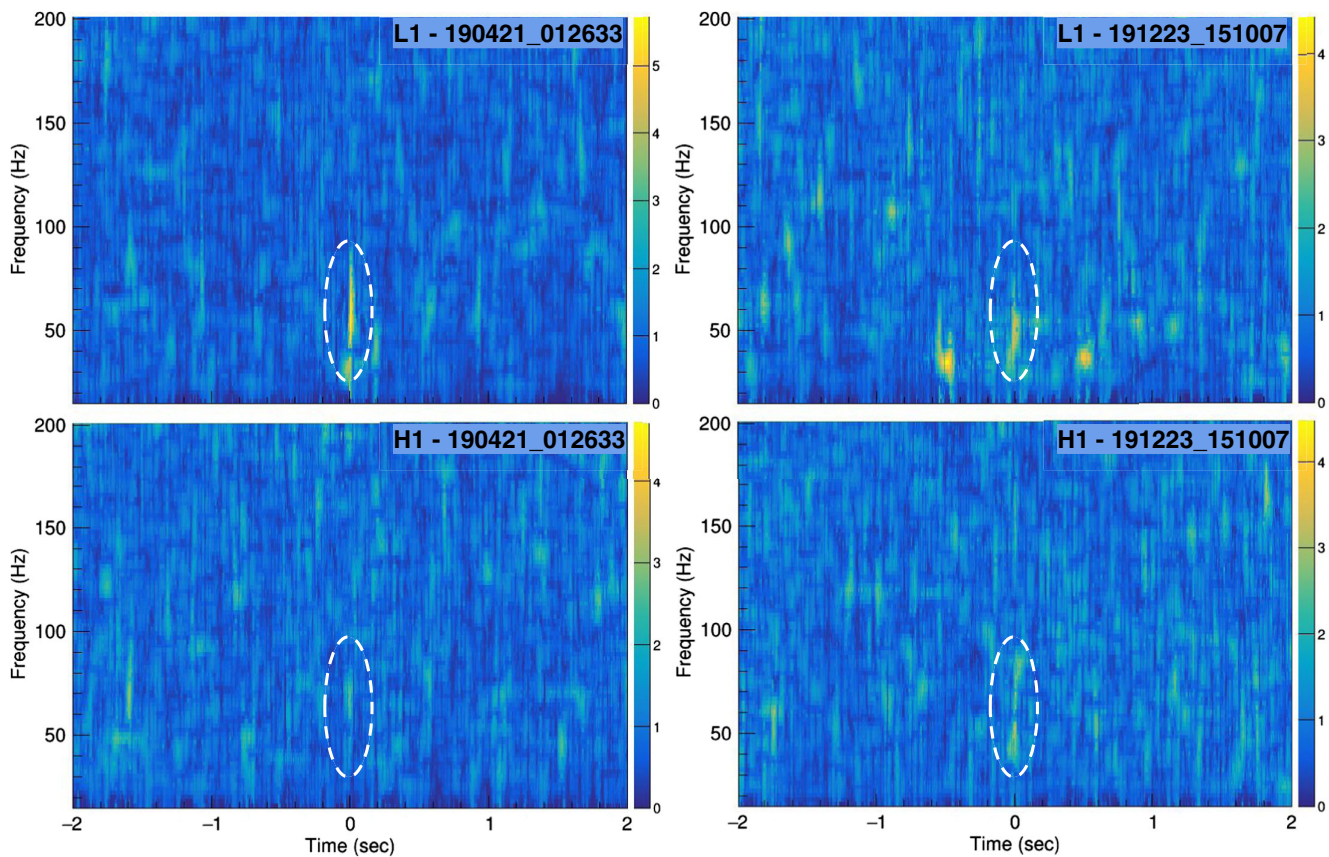
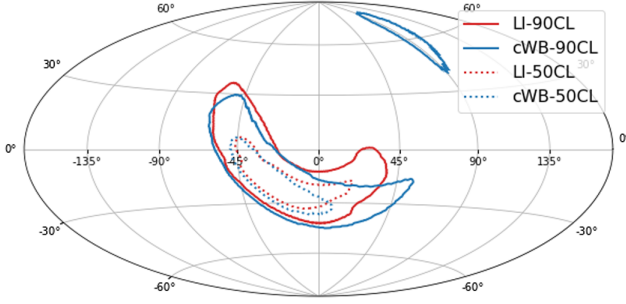


FIG. 1. Time-frequency wavescan spectrograms [47] of 190421_012633 (LEFT) and 191223_151007 (RIGHT), in the L1: Livingston (TOP) and H1: Hanford (BOTTOM) detectors. The marginal events occur at Time = 0 s in the plots and are highlighted by white dashed circles.

190421_012633



191223_151007

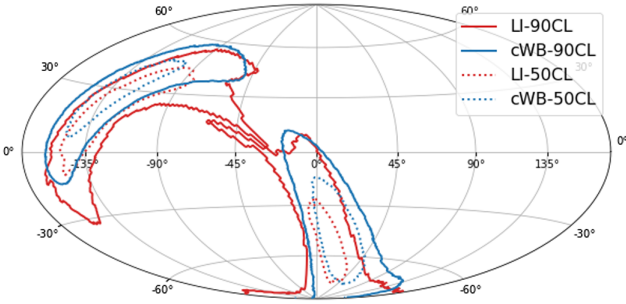


FIG. 2. The 90% and 50% credible sky localization area estimated by cWB [55] (Blue) vs the LAL Inference (LI) posterior distributions (Red), plotted for the marginal events 190421_012633 and 191223_151007.

We follow the XGBoost parameter estimation technique described in Ref. [27] and use their trained model to estimate the source frame total mass (M_{cWB}). The highest-ranked event 191223_151007 is estimated to have the M_{cWB} of $141 M_{\odot}$ with the P_{astro} value of 0.742. The standard cWB analysis had previously removed this event as it had failed the *a priori* defined veto thresholds on the event summary statistics. The event 190421_012633 was reconstructed in the standard cWB analysis with a FAR 7.1 yr^{-1} , and it was promoted by the ML-enhanced cWB search to a marginal event with a lower FAR. This event is estimated to have the M_{cWB} of $160 M_{\odot}$ with the P_{astro} value of 0.833.

In order to extract the source properties of the two marginal events, we perform the coherent Bayesian parameter estimation [48–50]. In this analysis, we model the GW signal as represented by a precessing quasicircular waveform IMRPhenomXPHM [51–54]. We report the median and 90% symmetric credible intervals for the one-dimensional marginal posterior distributions of the source total mass M and the source component masses m_1 and m_2 in Table III. The source frame total masses for both events are in agreement with the cWB estimated total masses. The secondary mass components fall within the stellar mass BBH range for both events, whereas the primary mass

components fall in the IMBH range with the source masses greater than $100 M_{\odot}$.

The sky localization area for the 190421_012633 and 191223_151007 marginal events are shown in Fig. 2. Here, the 90% credible sky area estimated by cWB [55] is consistent with the sky area inferred from the Bayesian posterior distribution. Although the low significance of these events is insufficient to claim confident detection, we have not identified them with any common instrumental noise origin.

C. Search sensitivity

The detection efficiency is calculated by taking the number of detected simulated events with FAR equal to or less than a given threshold and dividing it by the total number of recovered simulation events. From the detection efficiency vs FAR in Fig. 3, for FAR $< 1 \text{ yr}^{-1}$ ($< 1/100 \text{ yr}^{-1}$), we observe an 18% (16%) improvement

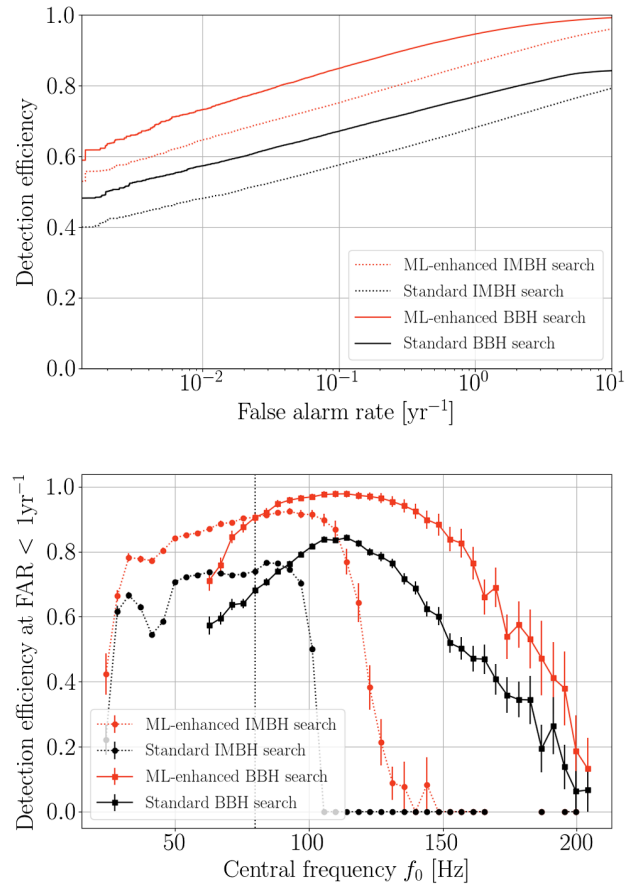


FIG. 3. Top: detection efficiency vs FAR for the O3 observing run. Bottom: detection efficiency for events identified with FAR less than 1 yr^{-1} as a function of the central frequency f_0 for O3. Solid lines correspond to the BBH configuration, while dotted lines represent the IMBH configuration. Red curves represent the sensitivity of the ML-enhanced cWB search, and black curves represent the sensitivity of the standard cWB search with the veto method.

TABLE IV. The effective hypervolume \mathcal{V} for the POWER LAW + PEAK population model injections over the O3 run, estimated at a FAR of 2 yr^{-1} . We compute the \mathcal{V} for the standard and ML-enhanced cWB searches over the O3a and O3b data. We compare the O3a hypervolumes for all the searches, including GstLAL, MBTA, PyCBC, and PyCBC BBH searches found in Ref. [4].

Run	Sensitive hypervolume \mathcal{V} ($\text{Gpc}^3 \text{ yr}$)					
	Standard cWB	ML-enhanced cWB	GstLAL	MBTA	PyCBC	PyCBC BBH
O3a	0.676	0.822	1.22	0.885	0.914	1.20
O3b	0.627	0.757

for both the BBH and IMBH configurations as compared to the standard cWB search. For simulated events detected with $\text{FAR} < 1 \text{ yr}^{-1}$, in Fig. 3 we plot the detection efficiency as a function of the central frequency f_0 . The overall ML-enhanced search is more sensitive than the standard search over the entire BBH mass range accessible by LIGO.

We compare the sensitivity of the ML-enhanced cWB pipeline with the other search pipelines by computing the sensitive hypervolume \mathcal{V} in units of volume \times time [4]. For this study, we choose the POWER LAW + PEAK model [4], which is a fiducial BBH population model with a high posterior probability in the population analysis of GW Transient Catalog 2 [32]. Given a local merger rate $R(z=0)$ and the observed number of detections N_{det} at a given significance threshold, we estimate the effective hypervolume \mathcal{V} by following the relation $N_{\text{det}} = \mathcal{V}R(z=0)$, where N_{det} is calculated by counting the number of injections detected by the search pipeline above a threshold at FAR 2 yr^{-1} . The effective hypervolume for

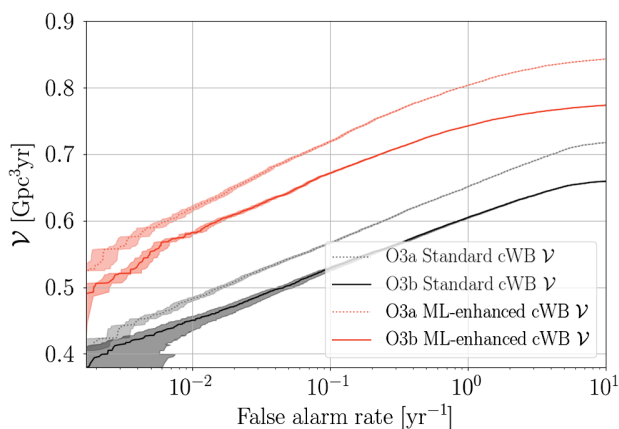


FIG. 4. Sensitive hypervolume \mathcal{V} plotted against FAR for O3 cWB searches using the BBH POWER LAW + PEAK simulations. Solid lines correspond to the O3b run, while dotted lines represent the O3a run. Red curves represent the sensitivity of the ML-enhanced cWB search, and black curves represent the sensitivity of the standard cWB search. The corresponding shaded regions denote the respective $1\text{-}\sigma$ confidence intervals on the FAR.

TABLE V. Percentage gain in the sensitive hypervolume (\mathcal{V}) by the ML-enhanced cWB search at FAR $< 1 \text{ yr}^{-1}$, $< 0.1 \text{ yr}^{-1}$, and FAR $< 0.01 \text{ yr}^{-1}$ for the BBH and IMBH search configurations.

Search	Percentage gain in \mathcal{V} with ML-enhanced cWB (%)		
	FAR $< 1 \text{ yr}^{-1}$	FAR $< 0.1 \text{ yr}^{-1}$	FAR $< 0.01 \text{ yr}^{-1}$
BBH	23.0	26.4	27.8
IMBH	26.5	30.3	34.2

each search for the given signal population is given in Table IV.

We note that the ML-enhanced cWB search improves the sensitive hypervolume by approximately 21% compared to the standard cWB search in Table IV. In the O3a run, the ML-enhanced cWB sensitive hypervolume is comparable to the MBTA search pipeline [4]. Figure 4 shows the sensitive hypervolume against FAR for the ML-enhanced cWB search and the standard cWB search for the O3a and O3b runs.

For the case of IMBH simulations, we do not use any IMBH population models and the injections are done over a uniform fiducial volume for different IMBH masses (II B). While we cannot quote the sensitive hypervolume for the IMBH search, we note that the fractional change in the sensitive hypervolume is approximately the same as the increase of detection efficiency with respect to injections. At FAR less than $1/100 \text{ yr}^{-1}$, the percentage increase in the sensitive hypervolume with the ML-enhanced cWB search is approximately 28% for the BBH search and 34% for the IMBH search as compared to the standard cWB search. The percentage gain for the BBH and IMBH search configurations with the ML-enhanced cWB search is reported for different FAR thresholds in Table V.

D. Test of robustness

The ML implementation is designed such that we maintain the model independent nature of the cWB search. The ML-enhanced search sensitivity is not limited to the simulations present in the training set [28]. In order to check this, we analyze the performance of the ML-enhanced search on simulated waveforms outside the training set. We train the ML model on quasi-circular binaries and test the ML-enhanced IMBH search sensitivity

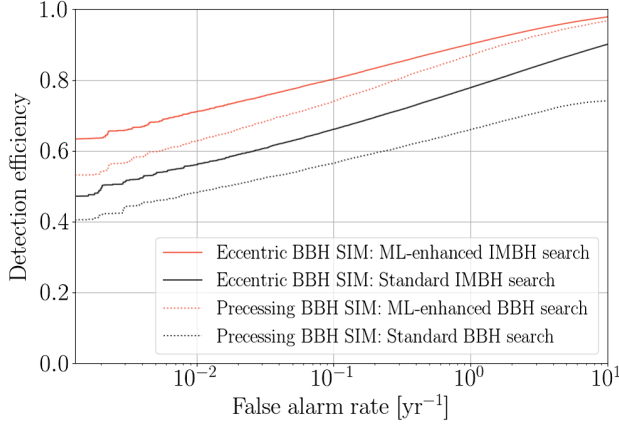


FIG. 5. Detection efficiency vs FAR for a high mass, eccentric BBH simulation set (solid lines), and a precessing BBH set (dotted lines) recovered with the cWB IMBH configuration, and BBH configuration respectively. The red curve represents the sensitivity of the ML-enhanced cWB search, and the black curve represents the sensitivity of the standard cWB search.

on high mass BBH systems with highly eccentric orbits (simulation set iii).

A similar test was conducted using precessing BBH systems (simulation set iv). The ML model is trained on simulated waveforms with the (2,2) harmonic mode, aligned spins, and low mass ratio (1–1/4). The testing set consists of simulated waveforms with higher-order modes, precessing spins, and a higher mass ratio (1–1/20).

In Fig. 5, we observe that the ML-enhanced search is more sensitive to the high mass eccentric BBH mergers and precessing BBH mergers despite the ML model being trained only on the quasicircular IMBH waveforms and BBH waveforms respectively. These results exhibit that the ML-enhanced search does not compromise the robustness of the standard search but rather improves the sensitivity of the search for BBH signals lying outside the training simulation set.

E. HL vs HLV

The Advanced Virgo detector joined the GW detector network in the later part of the O2 run. The addition of the Advanced Virgo detector to the existing two detector network (HL) allowed more precise sky localization of

the GW events. While ideally, adding a third detector is expected to improve the sensitivity, this is not usually the case seen in the cWB pipeline with the HL and HLV networks. With their common orientation, the LIGO detectors select a well-defined GW polarization state; that feature is exploited by cWB to mitigate their glitches. In contrast, the Virgo detector orientation differs considerably from that of the LIGO detectors so that glitches in Virgo data cannot be mitigated as efficiently by cWB. Therefore, the three-fold network including Virgo, with its current sensitivity level, is usually less sensitive than the HL network.

We test the ML-enhanced cWB search on limited data of the HLV network with the BBH search configuration. We train a model by using the accumulated background data and recovered simulations for the HLV network, on the limited data with live time interval—GPS:1241011102.0 to GPS:1242485126.0 which corresponds to ~ 7 days of live time taken from the first half of O3. For the HLV network, we use 550 years of background data for training. We end up with ~ 640 background years of the HLV network for testing the performance of the ML model. For the HL network, we use the BBH configuration trained model on the limited data. This exercise considers the total number of common injections made in the limited data live time for both the detector networks and compares their performance based on the recovered simulations at a given FAR as reported in Table VI. For the set of common injections in the HL (HLV) network, the ML-enhanced cWB search recovers around 23% (31%) more injections than the standard cWB search at $\text{FAR} < 1 \text{ yr}^{-1}$.

In Fig. 6, the detection efficiency is calculated as the ratio of the number of recovered simulations below a given FAR threshold to the total number of injections made in the limited data live time. We observe that the ML-enhanced cWB search improves the sensitivity for both HL and HLV networks. The HL network shows better performance and recovers $\sim 7.7\%$ more simulated events at $\text{FAR} < 1 \text{ yr}^{-1}$ as compared to the HLV network. In order to assess the performances of these two networks, we combine the HL and HLV network search results by applying a trial factor to the significance of events to check the HL + HLV network performance. We find that the joint search HL + HLV network recovers $\sim 3.0\%$ more simulations at

TABLE VI. Comparison of the number of recovered simulations by the ML-enhanced cWB search at $\text{FAR} < 1 \text{ yr}^{-1}$ and $\text{FAR} < 0.01 \text{ yr}^{-1}$ with respect to the total number of common injections made in limited data (corresponding to 7 days of live time in the O3 run) for both the HL and HLV detector networks.

Network	Injections	Recovered with Standard cWB		Recovered with ML-enhanced cWB	
		$\text{FAR} < 1 \text{ yr}^{-1}$	$\text{FAR} < 0.01 \text{ yr}^{-1}$	$\text{FAR} < 1 \text{ yr}^{-1}$	$\text{FAR} < 0.01 \text{ yr}^{-1}$
HL	5628	1475	1115	1818	1371
HLV	5628	1285	957	1688	1221
HL + HLV	5628	1548	1121	1873	1336

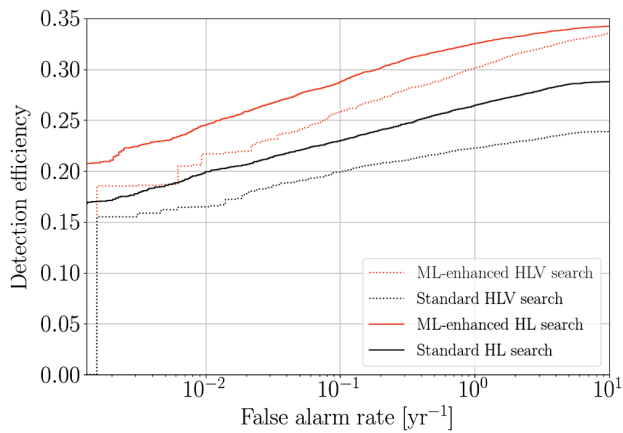


FIG. 6. The detection efficiency curves for HL and HLV networks calculated with respect to the total number of injections. The solid lines correspond to the HL network, whereas the dotted lines correspond to the HLV network. The black curves denote the performance of the standard cWB pipeline without ML, and the red curves denote the performance of the ML-enhanced cWB search. The steep drop of detection efficiency curves for the HLV network at low FAR is because of the limited background data (~ 640 years) available for testing.

FAR $< 1 \text{ yr}^{-1}$ than the HL network, and $\sim 11.0\%$ more simulations at FAR $< 1 \text{ yr}^{-1}$ than the HLV network. While adding Virgo to the HL network allows us to detect more events, the addition also increases the detector network's background noise, leading to a lower sensitivity at higher significance. For example, the HL network recovers $\sim 2.6\%$ more simulations at FAR $< 0.01 \text{ yr}^{-1}$ than the HL + HLV network. With the current cWB implementation and with Virgo lower sensitivity with respect to the LIGO detectors, it is still not beneficial to use the three-fold network for detection purposes. However, an improvement on the algorithmic side and/or on Virgo sensitivity, as well as the extension to a fourth detector, such as KAGRA, may soon change this condition. As a result, we utilize the best available (most sensitive) two-fold detector network.

IV. CONCLUSIONS

In this paper, we have successfully utilized the ML-enhanced cWB pipeline to search for BBH mergers in the third observing run (O3) of the Advanced LIGO-Virgo. The ML-enhanced cWB search consistently improves the search sensitivities, as previously presented in Ref. [28]. For simulated events with FAR $< 1/100 \text{ yr}^{-1}$, the sensitive hypervolume is improved by 28% for the stellar-mass BBH search configuration and by 34% for the IMBH search configuration. We recover with equivalent or higher significance, all the 15 + 10 (O3a+O3b) BBH events reported in the third GW Transient Catalog [6] that were previously detected by the standard cWB pipeline. The FAR assigned to the IMBH event GW190521 detected in the ML-enhanced cWB search is limited by the amount of available

accumulated background data, and it is two times more significant than the standard cWB search. Additionally, 5 GW events were detected by the ML-enhanced cWB search that were previously missed by the standard cWB search but detected by other search pipelines. Moreover, we detect three cWB-only candidate events with FAR $< 1 \text{ yr}^{-1}$ that are not present in the GW Transient Catalogs: 190904_174910, 190421_012633, and 191223_151007. The event 190904_174910 is found to be consistent with the instrumental noise produced around the 60 Hz line by the up-conversion of low-frequency seismic noise. The other two events, 190421_012633 and 191223_151007 are marginal IMBH candidates with their source frame total masses $> 100 M_{\odot}$ lying in the IMBH range. We find broad agreement between the inferred source frame total masses and the cWB estimates M_{cwb} for these two marginal events. Significant overlap in the 90% credible sky localization area estimated by cWB and given by the marginal posteriors is observed. While we have not identified any possible instrumental noise origin for these two events, the significance is insufficient to claim confident GW detection.

We also test the robustness of the ML implementation by training the ML models on quasicircular orbit binaries data and testing it on eccentric orbit binaries data, and precessing BBH data. We conclude that the ML-enhanced cWB search does not adversely affect the model independent nature of the cWB pipeline and improves the sensitivity of the pipeline to signals outside the training set.

Lastly, we perform a detector network comparison test, where we establish that the ML-enhanced cWB search enhances the search sensitivity for different detector networks. However, we also note that the HL detector network recovers $\sim 7.7\%$ more simulated events at FAR $< 1 \text{ yr}^{-1}$ than the HLV network. Plausible reasons for this are that the Virgo detector orientation differs considerably from that of the LIGO detectors and that the spectral amplitude noise has been about a factor 2 higher for Virgo with respect to LIGO.

As a future outlook, the ML-enhanced cWB pipeline will be used in the upcoming fourth observing run of LIGO, and further studies are being done to include this method in the low latency cWB search.

ACKNOWLEDGMENTS

This research has made use of data, software, and/or web tools obtained from the Gravitational Wave Open Science Center, a service of LIGO Laboratory, the LIGO Scientific Collaboration, and the Virgo Collaboration. This work was supported by the NSF Grants No. PHY 1806165 and No. PHY 2110060. We gratefully acknowledge the support of LIGO and Virgo for the provision of computational resources, especially LIGO Laboratory, which is supported by the NSF Grants No. PHY 0757058 and No. PHY 0823459. I. B. acknowledges support by the NSF Grant No. PHY 1911796, the Alfred P. Sloan Foundation, and by

the University of Florida. We acknowledge the use of open source PYTHON packages including NUMPY [56], PANDAS [57], MATPLOTLIB [58], and SCIKIT-LEARN [59].

APPENDIX: XGBOOST MODEL TRAINING UPDATES

In this section, we discuss all the updates made to the existing ML method as described in Ref. [28]. In order to account for the different detector networks, we replaced the summary statistic that described the quality of the likelihood fit (E_c/L) with (S_0/L) for the two detector network (HL), and with $(S_0/L$ and $S_1/L)$ for the three detector network (HLV). The summary statistics gives the ratio of the square of the SNR of the reconstructed waveform for each detector (S_0, S_1) to the likelihood (L). This allows us to increase the sensitivity of the ML algorithm to different detector networks. The detailed list of selected summary statistics and their definitions can be found in the Appendix of Ref. [28].

The XGBoost hyperparameters, listed in Table VII, were carefully selected to avoid overfitting and for optimal performance with O3a data for both the BBH and IMBH search configurations. In this study, we first start by setting all XGBoost hyperparameters to be the same as used for O1 and O2 analysis. We then select *a priori*, the `max_depth` to 13 as we use 13 cWB summary statistics in the list of input features. We also set the `colsample_bytree` to 1, *a priori*, which ensures that all the features are used while building each tree in the ensemble, during training. Then we perform a short grid search over 9 combinations of XGBoost hyperparameters with respect to the precision-recall area under the curve (AUC PR) metric [60], and fix the `subsample` and `gamma` as reported in Table VII. The total number of trees generated is optimized by using a method known as *early stopping*, where a small fraction of the training data set is set aside for validation, and the training ends when the validation score with respect to AUC PR metric stops

TABLE VII. Entries for XGBoost hyperparameters. †: `n_estimators` is optimized using early stopping, where the training stops when the validation score stops improving. Bold entries indicate the optimal choice.

XGBoost hyperparameter	Entry
<code>objective</code>	<code>binary:logistic</code>
<code>tree_method</code>	<code>hist</code>
<code>grow_policy</code>	<code>lossguide</code>
<code>n_estimators</code>	20,000†
<code>max_depth</code>	13
<code>learning_rate</code>	0.03
<code>min_child_weight</code>	10.0
<code>colsample_bytree</code>	1.0
<code>subsample</code>	0.4, 0.6 , 0.8
<code>gamma</code>	2.0 , 5.0, 10.0

improving with additional trees. This prevents overfitting of the XGBoost algorithm to the training data.

The ML algorithm is computationally efficient and the entire training and testing procedure is completed within minutes, using one CPU core. In order to get rid of excess background with minimal or no loss of simulated events, we employ a cutoff on the η_0 statistic with the threshold set at $\eta_0 > 6.5$. Before we use this summary statistic as an input feature for XGBoost training, we cap the statistic at $\eta_0 = 20$ (which was earlier set to 8 because of the previous η_0 definition in the paper [28]) such that any event with a higher η_0 value is assigned a value of 20. The capping prevents the algorithm from being affected by high SNR background events, which fall steeply with the increase in η_0 .

In addition to using η_0 as an input feature for XGBoost, we also apply a η_0 dependent sample weight on the background events to minimize the importance given by the algorithm to low SNR glitches. A standardized sample weight has been proposed in this work as compared to the one reported in Ref. [28]. All the simulation events are assigned a sample weight of 1. In contrast, for the noise events, we first divide simulation events in the interval $6.5 < \eta_0 < 20$ into `nbins = 100` percentile bins such that the number of simulation events in each bin is the same. Then, we apply the sample weight per bin as follows:

$$w_B(i) = \frac{N_S(i)}{N_B(i)} e^{\ln(A)(1-\frac{i}{\text{nbins}})^q}, \quad (\text{A1})$$

where, $i = 0, 1, \dots, \text{nbins}$ is a given bin, $N_S(i)$ and $N_B(i)$ are the number of simulation and background events in the i th bin. (q, A) are weight options, where A is called the balance parameter and it sets the class balance (N_B/N_S) for the first bin at $\eta_0 \geq 6.5$ (for instance $A = 100$ implies that the weighted background is 100 times more than the simulation in the first bin), q is called the slope parameter that controls the rate of change of the weighted background

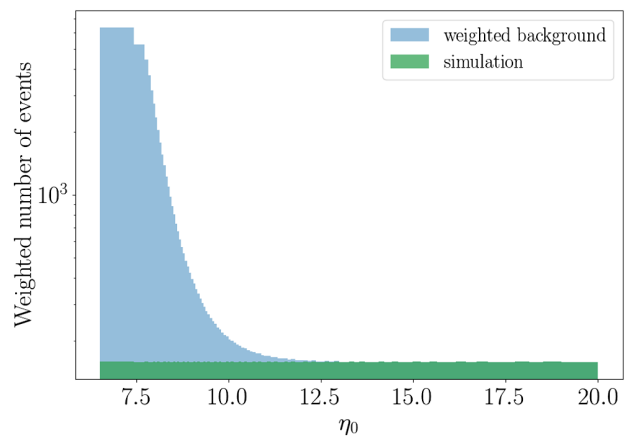


FIG. 7. Weighted event distribution as a function of η_0 for O3a run BBH search configuration data. The weight options are set to $q = 5$ and $A = 40$.

distribution. For all events with $\eta_0 \geq 20$, the number of simulation events is resampled such that it matches the number of background events to attain a perfect class balance ($N_B/N_S = 1$). For a given combination of (q, A) values, we can achieve any monotonic distribution of our choice, starting with a class balance of A at $\eta_0 = 6.5$ and

ending with a perfect class balance at $\eta_0 = 20$. In this study, the weight options were fixed to be $q = 5$ and $A = 40$, resulting in a weighted distribution as shown in Fig. 7. This weight distribution enables the ML model to differentiate high SNR events into noise and signal, while at the same time being sensitive to low SNR events.

-
- [1] J. Aasi *et al.* (LIGO Scientific Collaboration), *Classical Quantum Gravity* **32**, 074001 (2015).
- [2] F. Acernese *et al.* (Virgo Collaboration), *Classical Quantum Gravity* **32**, 024001 (2015).
- [3] B. P. Abbott *et al.* (LIGO Scientific, Virgo Collaborations), *Phys. Rev. X* **9**, 031040 (2019).
- [4] R. Abbott *et al.* (LIGO Scientific, Virgo Collaborations), *Phys. Rev. X* **11**, 021053 (2021).
- [5] R. Abbott *et al.* (LIGO Scientific, VIRGO Collaborations), [arXiv:2108.01045](https://arxiv.org/abs/2108.01045).
- [6] R. Abbott *et al.* (LIGO Scientific, VIRGO, KAGRA Collaborations), [arXiv:2111.03606](https://arxiv.org/abs/2111.03606).
- [7] K. Cannon *et al.*, *SoftwareX* **14**, 100680 (2021).
- [8] C. Hanna *et al.*, *Phys. Rev. D* **101**, 022003 (2020).
- [9] C. Messick *et al.*, *Phys. Rev. D* **95**, 042001 (2017).
- [10] G. S. Davies, T. Dent, M. Tápai, I. Harry, C. McIsaac, and A. H. Nitz, *Phys. Rev. D* **102**, 022004 (2020).
- [11] T. Adams, D. Buskulic, V. Germain, G. M. Guidi, F. Marion, M. Montani, B. Mours, F. Piergiovanni, and G. Wang, *Classical Quantum Gravity* **33**, 175012 (2016).
- [12] S. A. Usman *et al.*, *Classical Quantum Gravity* **33**, 215004 (2016).
- [13] F. Aubin *et al.*, *Classical Quantum Gravity* **38**, 095004 (2021).
- [14] S. Klimenko, I. Yakushin, A. Mercer, and G. Mitselmakher, *Classical Quantum Gravity* **25**, 114029 (2008).
- [15] S. Klimenko, G. Vedovato, M. Drago, F. Salemi, V. Tiwari, G. A. Prodi, C. Lazzaro, K. Ackley, S. Tiwari, C. F. Da Silva, and G. Mitselmakher, *Phys. Rev. D* **93**, 042004 (2016).
- [16] M. Drago, S. Klimenko, C. Lazzaro, E. Milotti, G. Mitselmakher, V. Necula, B. O'Brien, G. A. Prodi, F. Salemi, M. Szczepanczyk, S. Tiwari, V. Tiwari, G. V. G. Vedovato, and I. Yakushin, *SoftwareX* **14**, 100678 (2021).
- [17] S. Klimenko, G. Vedovato, V. Necula, F. Salemi, M. Drago, R. Poulton, E. Chassande-Mottin, V. Tiwari, C. Lazzaro, B. O'Brien, M. Szczepanczyk, S. Tiwari, and V. Gayathri, cWB pipeline library: 6.4.1 (2021), [10.5281/zenodo.5798976](https://zenodo.org/record/5798976).
- [18] cWB Development Team, coherent WaveBurst Homepage (2021), <https://gwburst.gitlab.io/>.
- [19] B. P. Abbott *et al.* (LIGO Scientific, Virgo Collaborations), *Phys. Rev. Lett.* **116**, 061102 (2016).
- [20] R. Abbott *et al.* (LIGO Scientific, Virgo Collaborations), *Astrophys. J. Lett.* **896**, L44 (2020).
- [21] G. Vedovato, E. Milotti, G. A. Prodi, S. Bini, M. Drago, V. Gayathri, O. Halim, C. Lazzaro, D. Lopez, A. Miani, B. O'Brien, F. Salemi, M. Szczepanczyk, S. Tiwari, A. Virtuoso, and S. Klimenko, *Classical Quantum Gravity* **39**, 045001 (2021).
- [22] B. P. Abbott *et al.* (LIGO Scientific, Virgo Collaborations), *Phys. Rev. Lett.* **125**, 101102 (2020).
- [23] M. Szczepanczyk, S. Klimenko, B. O'Brien, I. Bartos, V. Gayathri, G. Mitselmakher, G. Prodi, G. Vedovato, C. Lazzaro, E. Milotti, F. Salemi, M. Drago, and S. Tiwari, *Phys. Rev. D* **103**, 082002 (2021).
- [24] S. Vinciguerra, M. Drago, G. A. Prodi, S. Klimenko, C. Lazzaro, V. Necula, F. Salemi, V. Tiwari, M. C. Tringali, and G. Vedovato, *Classical Quantum Gravity* **34**, 094003 (2017).
- [25] M. Cavaglià, S. Gaudio, T. Hansen, K. Staats, M. Szczepanczyk, and M. Zanolin, *Mach. Learn.* **1**, 015005 (2020).
- [26] V. Gayathri, D. Lopez, I. S. Heng, A. Pai, and C. Messenger, *Phys. Rev. D* **102**, 104023 (2020).
- [27] B. O'Brien, M. Szczepanczyk, V. Gayathri, I. Bartos, G. Vedovato, G. Prodi, G. Mitselmakher, and S. Klimenko, *Phys. Rev. D* **104**, 082003 (2021).
- [28] T. Mishra, B. O'Brien, V. Gayathri, M. Szczepanczyk, S. Bhaumik, I. Bartos, and S. Klimenko, *Phys. Rev. D* **104**, 023014 (2021).
- [29] LIGO Scientific Collaboration and Virgo Collaboration, LIGO Virgo strain data from GWTC-3 catalog (2021), <https://www.gw-openscience.org/GWTC-3/>.
- [30] V. Necula, S. Klimenko, and G. Mitselmakher, *J. Phys. Conf. Ser.* **363**, 012032 (2012).
- [31] V. Gayathri, P. Bacon, A. Pai, E. Chassande-Mottin, F. Salemi, and G. Vedovato, *Phys. Rev. D* **100**, 124022 (2019).
- [32] R. Abbott *et al.* (LIGO Scientific, Virgo Collaborations), *Astrophys. J. Lett.* **913**, L7 (2021).
- [33] B. P. Abbott *et al.*, *Astrophys. J.* **900**, L13 (2020).
- [34] P. A. R. Ade *et al.*, *Astron. Astrophys.* **594**, A13 (2016).
- [35] E. D. Kovetz, I. Cholis, P. C. Breyse, and M. Kamionkowski, *Phys. Rev. D* **95**, 103010 (2017).
- [36] C. Talbot and E. Thrane, *Astrophys. J.* **856**, 173 (2018).
- [37] A. Bohé *et al.*, *Phys. Rev. D* **95**, 044028 (2017).
- [38] B. P. Abbott *et al.* (LIGO Scientific, Virgo Collaborations), *Phys. Rev. D* **100**, 064064 (2019).
- [39] J. Healy, C. O. Lousto, Y. Zlochower, and M. Campanelli, *Classical Quantum Gravity* **34**, 224001 (2017).
- [40] V. Gayathri, J. Healy, J. Lange, B. O'Brien, M. Szczepanczyk, I. Bartos, M. Campanelli, S. Klimenko, C. Lousto, and R. O'Shaughnessy, *Nat. Astron.* **6**, 344 (2022).
- [41] S. Ossokine *et al.*, *Phys. Rev. D* **102**, 044055 (2020).

- [42] T. Chen and C. Guestrin, in *Proceedings of the 22nd ACM SIGKDD International Conference on Knowledge Discovery and Data Mining*, KDD '16 (Association for Computing Machinery, New York, NY, USA, 2016), p. 785–794, [10.1145/2939672.2939785](https://doi.org/10.1145/2939672.2939785).
- [43] W. M. Farr, J. R. Gair, I. Mandel, and C. Cutler, *Phys. Rev. D* **91**, 023005 (2015).
- [44] J. C. Driggers *et al.* (LIGO Scientific Collaboration), *Phys. Rev. D* **99**, 042001 (2019).
- [45] D. Davis, T. J. Massinger, A. P. Lundgren, J. C. Driggers, A. L. Urban, and L. K. Nuttall, *Classical Quantum Gravity* **36**, 055011 (2019).
- [46] G. Vajente, Y. Huang, M. Isi, J. C. Driggers, J. S. Kissel, M. J. Szczepanczyk, and S. Vitale, *Phys. Rev. D* **101**, 042003 (2020).
- [47] S. Klimentko, [arXiv:2201.01096](https://arxiv.org/abs/2201.01096).
- [48] J. Veitch *et al.*, *Phys. Rev. D* **91**, 042003 (2015).
- [49] J. Lange *et al.*, *Phys. Rev. D* **96**, 104041 (2017).
- [50] D. Wysocki, R. O’Shaughnessy, J. Lange, and Y.-L. L. Fang, *Phys. Rev. D* **99**, 084026 (2019).
- [51] G. Pratten, C. García-Quirós, M. Colleoni, A. Ramos-Buades, H. Estellés, M. Mateu-Lucena, R. Jaume, M. Haney, D. Keitel, J. E. Thompson, and S. Husa, *Phys. Rev. D* **103**, 104056 (2021).
- [52] G. Pratten, S. Husa, C. Garcia-Quiros, M. Colleoni, A. Ramos-Buades, H. Estelles, and R. Jaume, *Phys. Rev. D* **102**, 064001 (2020).
- [53] C. García-Quirós, M. Colleoni, S. Husa, H. Estellés, G. Pratten, A. Ramos-Buades, M. Mateu-Lucena, and R. Jaume, *Phys. Rev. D* **102**, 064002 (2020).
- [54] C. García-Quirós, S. Husa, M. Mateu-Lucena, and A. Borchers, *Classical Quantum Gravity* **38**, 015006 (2021).
- [55] R. Essick, S. Vitale, E. Katsavounidis, G. Vedovato, and S. Klimentko, *Astrophys. J.* **800**, 81 (2015).
- [56] C. R. Harris *et al.*, *Nature (London)* **585**, 357 (2020).
- [57] pandas-dev/pandas: Pandas (2020).
- [58] J. D. Hunter, *Comput. Sci. Eng.* **9**, 90 (2007).
- [59] F. Pedregosa *et al.*, *J. Mach. Learn. Res.* **12**, 2825 (2011), <https://dl.acm.org/doi/10.5555/1953048.2078195>.
- [60] J. Davis and M. Goadrich, in *Proceedings of the 23rd international conference on Machine learning—ICML 06* (Association for Computing Machinery, New York, NY, USA, 2006), [10.1145/1143844.1143874](https://doi.org/10.1145/1143844.1143874).